J. Phys. D: Appl. Phys. **29** (1996) 133–146. Printed in the UK

Phase objects in synchrotron radiation hard x-ray imaging

Peter Cloetens†§, Raymond Barrett†, José Baruchel†, Jean-Pierre Guigay‡ and Michel Schlenker‡

† ESRF, BP 220, 38043 Grenoble, France
‡ Laboratoire Louis Néel du CNRS/UJF, BP 166, 38042 Grenoble Cedex 9, France

Received 14 August 1995

Abstract. Phase objects are readily imaged through Fresnel diffraction in the hard x-ray beams of third-generation synchrotron radiation sources such as the ESRF, due essentially to the very small angular size of the source. Phase objects can lead to spurious contrast in x-ray diffraction images (topographs) of crystals. It is shown that this contrast can be eliminated through random phase plates, which provide an effective way of tailoring the angular size of the source. The possibilities of this very simple technique for imaging phase objects in the hard x-ray range are explored experimentally and discussed. They appear very promising, as shown in particular by the example of a piece of human vertebra, and could be extended to phase tomography.

1. Introduction

Imaging is performed with a variety of probes, including light and electrons, but also NMR-frequency electromagnetic waves, ultrasound, x-rays and neutrons. All these techniques have developed because each probe has its merits in terms either of resolution or of the scale of the samples that it can handle and provides original information related to the physical quantities to which it is sensitive. Soft x-ray microscopy (wavelength range of the order of 100 Å) has recently developed into a technique with high resolution [1]. It includes phase contrast possibilities and appears to be very useful in the investigation of biological objects [2].

Hard x-rays ($\lambda < 2$ Å) are commonly used for imagery in two ways. Radiography, in which the basis for contrast is inhomogeneous absorption in simple transmission, is extremely widespread both in industrial testing and in medicine, and includes sophisticated variants such as computer-aided tomography. In x-ray diffraction imaging (usually called x-ray topography), inhomogeneities in Bragg diffraction reflectivity make it possible to image defects in single crystals [3]. Related techniques exist in the case of neutrons [4, 5].

X-ray phase imaging in this wavelength range was pioneered by Hosoya *et al* [6] using a Bonse–Hart type interferometer, consisting of several slices of perfect crystal silicon, acting as a coherent splitter, deviators and recombiner, carved out of a monolithic single-crystal block. In this case differences in optical path for the beam transmitted through an object are directly converted, after interference with the reference beam, into inhomogeneous intensity, hence contrast. The same principle was applied with neutrons by Schlenker *et al* [7], who also showed that, after suppression of the reference beam, the phase jumps or gradients remain visible. Similar techniques, in which a sample is placed between the two crystal slabs of a Bonse–Hart small-angle scattering camera and phase gradients are visualized essentially through refraction, were used by Förster *et al* [8] and several other groups [9] with x-rays and by Podurets *et al* [10] in the neutron case.

Free-space propagation can also transform the phase modulation of the incident beam into an amplitude modulation. This imaging process was recently studied extensively both experimentally and theoretically by Snigirev *et al* [11] at the European Synchrotron Radiation Facility (ESRF, Grenoble). It may be described as a refraction phenomenon or more generally, in a wave-optical approach, as Fresnel diffraction.

We first encountered this effect during x-ray topographic work at the ESRF in the form of spurious images, obviously not related to the crystals under investigation. Figure 1 shows a topograph taken at x-ray energy 26 keV (wavelength $\lambda = 0.48$ Å), of a rather perfect KTP crystal, which exhibits some surface defects, dislocations and growth bands. Apart from these crystal defects, a set of horizontal lines is very clearly visible: they were traced to slight rolling defects in a beryllium window placed across the beamline 2.8 m upstream of the sample. At the photon energy used, the absorption of the beryllium window is negligible and the image is due to the variations in optical pathlength, hence of phase, associated with the variations in thickness.

We then investigated the possibilities of deliberately imaging phase objects with this technique of Fresnel

§ Research assistant for the National Fund for Scientific Research of Belgium.

0022-3727/96/010133+14$19.50

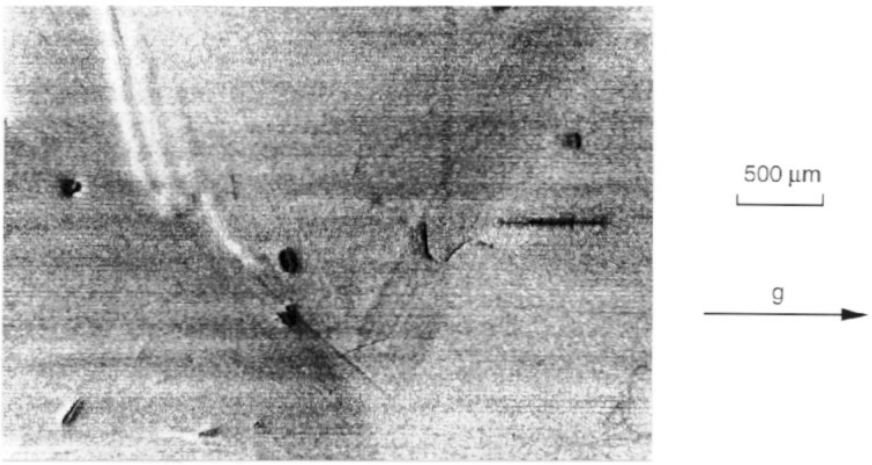

Figure 1. An x-ray diffraction image (topograph) of a KTP crystal. Crystal defects are visible as well as horizontal lines due to rolling defects in a beryllium window, 2.8 m upstream with respect to the film. It is a monochromatic beam topograph in transmission; reflections 111 (monochromator) and 004 (crystal under study); E = 26 keV (λ = 0.48 Å).

imaging. Although it is based on the coherence properties of x-ray beams from a highly sophisticated third-generation synchrotron source with very low emittance, it is to be noted that this method is extremely simple and involves almost no instrumentation. We also sought a way of suppressing the spurious images on x-ray topographs.

2. Phase imaging

2.1. Experimental results

Figure 2 shows the typical experimental set-up used for imaging, either in the topographic mode or for the Fresnel diffraction imaging of phase objects. We used the Optics Beamline (D5) at ESRF, whose 0.8 T bending magnet gives an effective source size of the order of 300 μm in the vertical direction and 600 μm horizontally, at a distance of 60 m from the crystal C. The very low divergence synchrotron radiation white beam, restricted in width and height by a set of slits, is diffracted by the single crystal C, and the diffracted beams are recorded on photographic film F. Situations in which harmonics occur, such as wavelength λ being diffracted by the Bragg reflection hkl and wavelength $\lambda/2$ by the reflection $2h$, $2k$, $2l$ into the same direction, were avoided in our experiments.

In the standard white beam topographic approach, each of the diffracted beams, hence each spot of the Laue pattern thus obtained, is an image which shows defects in C through local variations in the diffracted intensity. Alternatively, a film can be placed across just one of the diffracted beams, in particular if a large specimen-to-film distance is required. This set-up can also be considered just as a way of extracting one or several narrow spectral bands (typically $\Delta\lambda/\lambda \simeq 10^{-5}$) out of the white beam. Images were recorded on Kodak Industrex SR or SO-343 x-ray film, with exposure times of the order of 1 s.

When C is perfect and has uniform thickness, no contrast is normally obtained within the spots. However, when a phase object is placed, deliberately or not, across the beam, it is found that features of the phase object can be strikingly imaged on the film. C can be set to diffract either in Laue (transmission) or in Bragg (reflection) geometry.

Figure 3 shows the image obtained when two crossed polymer strings with an outer diameter of 0.7 mm were placed downstream of a perfect 4.5 mm thick silicon crystal, mechano-chemically polished, set in symmetrical Bragg geometry for the 111 reflection, with an object–film distance (subsequently referred to as D) of 100 cm. The picture was obtained using a diffracted beam in the horizontal plane with energy 18.8 keV ($\lambda = 0.66$ Å). At this energy the maximum absorption is less than 5% for the string as a whole and less than 0.02% for the individual 20 μm diameter fibres constituting the string. Thus contrast is again due to the phase modulation, i.e. to the real part of the refractive index. The topographic image shows residual polishing damage on the crystal surface. The strings and fibres are clearly visible. The visible features are mainly the edges, namely the parts where refraction or equivalently the phase gradient are greatest. When the film is placed against the object, no contrast is obtained from the strings. This unambiguously ascribes the image formation to free-space propagation, or alternatively Fresnel diffraction, in exact analogy to the defocusing method for imaging phase objects in electron microscopy [12], but with the obvious difference that in this x-ray case the only non-defocused position is that of the object itself, because focusing optics are not commonly available in hard x-ray work.

As previously noted, an alternative way to visualize the phase gradients created by the object is to use a second, analyser, crystal downstream of the object to act as an angular filter; that is, to perform Schlieren imaging as reported by Förster *et al* [8]. To compare the contrast obtained with the simple free-space propagation technique and this more conventional configuration, objects were placed between two silicon crystals in $(n, -n)$ Laue configuration at an x-ray energy 31 keV ($\lambda = 0.4$ Å), 111 reflection. Rotation of the second crystal allows an angular selection of the waves coming from the object

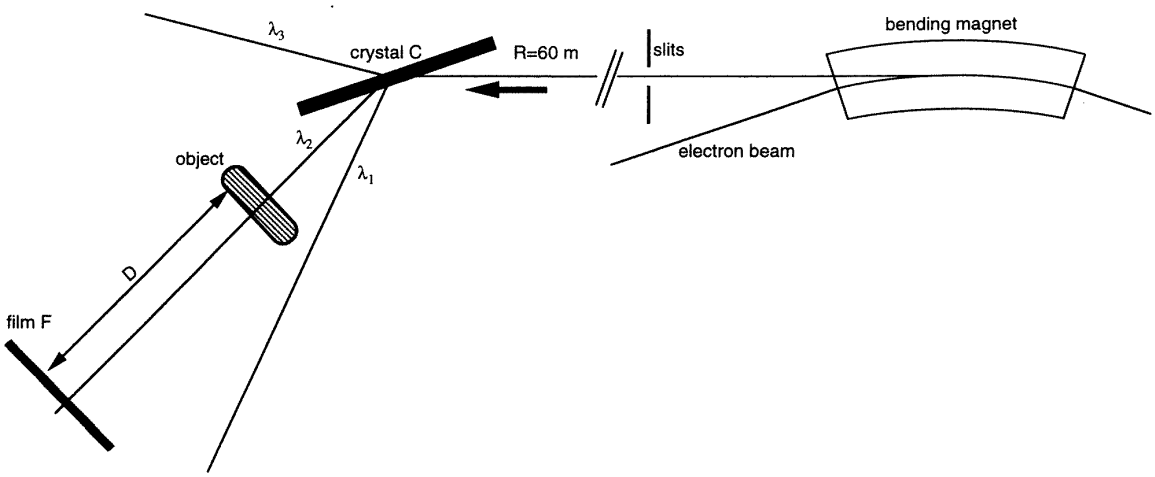

Figure 2. The experimental set-up for white beam topography and phase-imaging. Polychromatic synchrotron radiation from a bending magnet falls on a fairly perfect crystal C at 60 m from the source. Monochromatic ($\Delta\lambda/\lambda \approx 10^{-5}$) beams with different wavelengths are diffracted in several directions, each of which forms an image of the crystal. For phase-imaging, an object is placed in the beam (downstream or upstream with respect to the crystal) and an image is recorded at object–film distance, D.

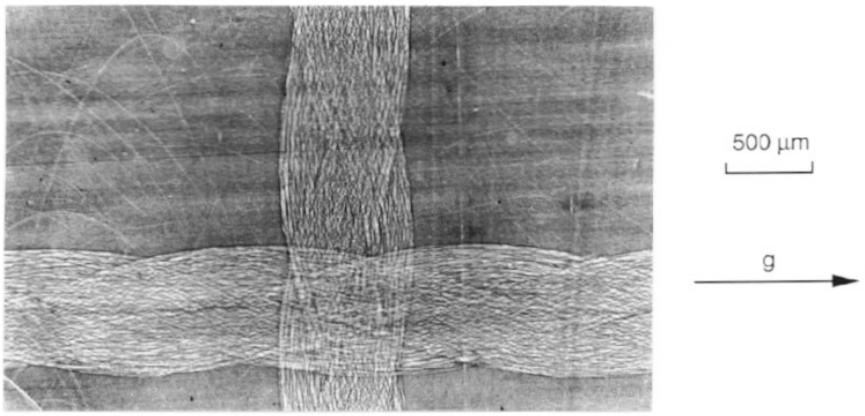

Figure 3. Two crossed polymer strings, i.e. low absorbing objects, downstream of the monochromator. Edges of the object appear with high contrast when the photographic plate is placed at a distance D = 100 cm behind the object. Symmetric Bragg reflection: 111; E = 18.8 keV (λ = 0.66 Å).

corresponding to the angular acceptance of the analyser crystal and its position relative to the monochromator. Figures 4(a) and (b) show the string and a 100 μm diameter nylon fibre with an angular displacement between the rocking curve maxima of the monochromator and analyser crystal of respectively 0 and 8.7 μrad (1.8″). In figure 4(a) the edges appear white (this means less intensity) because the rays are deviated in this region away from the Bragg condition. In figure 4(b) at the left-hand edge the deviation by the object brings the rays closer to the exact Bragg condition and does the opposite at the symmetrical edges. The contrast formation in this method has been treated previously by Förster *et al* [8] and Goetz *et al* [13]. The small angular source size and high brilliance at the ESRF simplifies the experimental set-up with respect to the earlier experiments done with classical x-ray sources; the fundamental spatial resolution limit imposed by the interaction of the x-ray wavefield with the analyser crystal downstream of the object remains unchanged. As discussed later, the free-space propagation technique need not be limited in the same way.

Figures 5(a)–(c) show images of a slice of obeche (*Triplochiton scleroxylon* K Schum) wood obtained using the single crystal configuration (figure 2) at 18.8 keV at respectively D = 5, 50 and 100 cm. The slice, cut transversely (perpendicular to the fibres) from a commercial curtain rod, was approximately 2 mm thick and completely rough on one side. Clearly the image is strongly affected by the object–film propagation distance D, and the spatial frequencies f which are visible appear to decrease with increasing distance. In this case, similar features are visible with this technique and with optical microscopy, the difference being that the x-ray image is obtained in transmission.

Figures 6(a) and (b) show images of a 7 mm thick slice from a human vertebra, placed downstream of a silicon

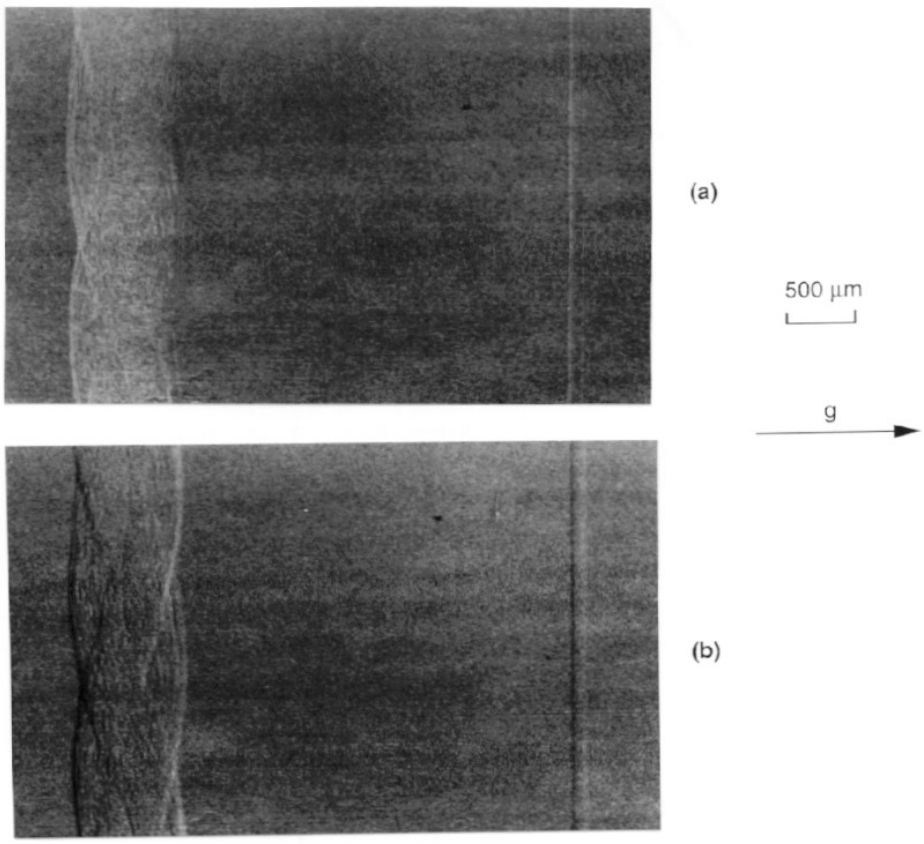

Figure 4. Schlieren imaging performed by placing a polymer string and a 100 μm diameter nylon fibre (visible at the right-hand side) between two silicon crystals in $(n, -n)$ configuration: (*a*) on the peak of the rocking curve and (*b*) 8.7 μrad (1.8″) away from the peak. Symmetric Laue reflections: 111; E = 30 keV (λ = 0.41 Å).

monochromator in symmetric Bragg reflection, obtained at 18.8 keV with D respectively 0 and 1 m. The image in figure 6(*a*) is entirely due to absorption; the image in figure 6(*b*) is due to both absorption and phase imaging. Because the phase imaging process enhances the visibility of discontinuities in the object, the image in figure 6(*b*) gives the impression of being sharper, but also reveals many details of the bone structure that are simply indistinguishable in the absorption image.

Probably the simplest possible phase object consists of a phase step, for which the edge of a 60 μm thick silicon crystal was used and set perpendicular to the monochromatic beam delivered by a horizontally diffracting perfect silicon crystal in Laue geometry. At the photon energy used, 31 keV ($\lambda = 0.4$ Å), this represents a phase jump close to $-3\pi/2$. The image was recorded at a distance $D = 117$ cm. The absorption in the sample is 1.8%, and cannot explain the contrast at the horizontal edge. Figure 7(*a*) shows the intensity profile as measured for a slightly tilted edge (tilt 4.5°), schematically represented in the insert. The profile was obtained by digitizing the film and projecting parallel to the edge. The maximum of the intensity is on the air side, as may be expected from refraction at the thin part of the crystal set at a small angle with respect to the beam. Figure 7(*b*) shows the profile for a nearly perpendicular edge, represented in the insert. The black/white/black contrast cannot be explained geometrically, but is quite familiar as a Fresnel diffraction phenomenon. The central minimum is due to destructive interference of waves coming from points symmetrical with respect to the edge and the oscillations are Fresnel fringes. The very simplicity of this object gives the possibility of quantitative evaluation. The measured distance between the two maxima of 12.1($\pm$0.6) μm is in good agreement with the theoretical value of $1.7(\lambda D)^{1/2} = 11.6$ μm [14], $(\lambda D)^{1/2}$ being the radius of the first Fresnel zone. The visibility of the fringes depends on the angular size of the source. From simulations we may estimate the vertical effective source size to be 170 μm, which is to be compared to the earlier mentioned value of 300 μm. The dissymmetry between the two maxima (opposite to the expected dissymmetry from the value of the phase jump) could be explained by a slight deviation from perpendicularity of the crystal with respect to the beam, or by dust deposited on the edge. Here again it is clear that this method does not give a uniform change in intensity for the part of the beam passing through the crystal, as would be the case for an absorption image if the sample absorbed more, or for an interferometric phase image. The immediately obvious edge enhancement is, under closer examination, revealed to derive from the theoretically expected fringe structure.

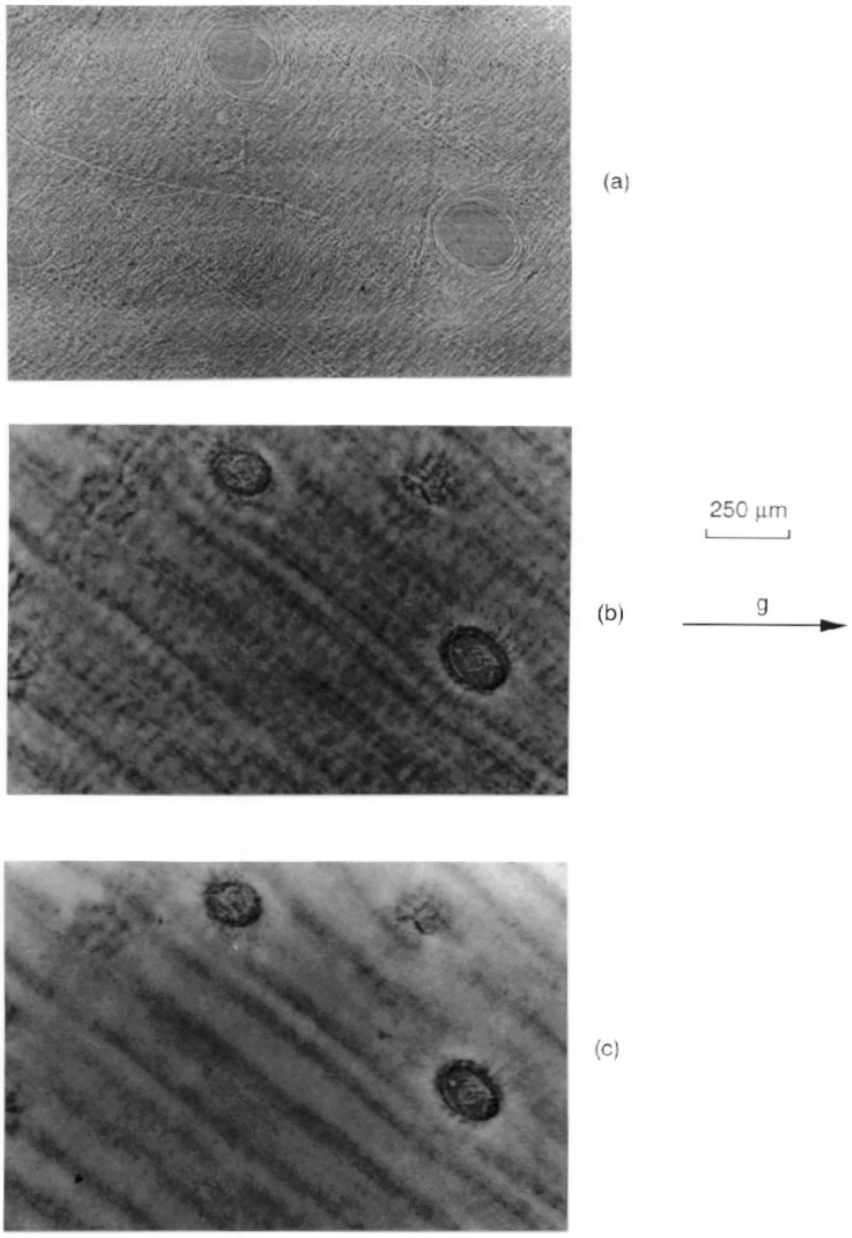

Figure 5. A sample of obeche wood (*Triplochiton scleroxylon* K Schum), 2 mm thick transverse cut, downstream of the monochromator. The aspect of the image is strongly dependent on the recording distance: (*a*) D = 0.05 m, (*b*) D = 0.5 m and (*c*) D = 1 m. The spatial frequencies f which are visible appear to decrease with increasing distance. Symmetric Bragg reflection: 111; E = 18.8 keV (λ = 0.66 Å).

2.2. Basic elements of the imaging process

The contrast described above could be explained in a ray-optical approach by refraction of the rays in the object. These very small deviations in the propagation direction (of the order of 10 μrad) are sufficient to create visible intensity variations after propagation of the rays in air over a distance of the order of 1 m. A more general and accurate description of the contrast formation is given by a wave-optical approach. The object can be characterized in a scalar approximation by its complex transmission function F [15] such that

$$u(x, y) = F(x, y)u_0(x, y) \tag{1}$$

where u and u_0 denote the monochromatic field respectively just downstream and upstream of the object at the point (x, y) of the object plane. This transmission function F involves the real and the imaginary part of the index of refraction in the object and can be expressed as

$$F(x, y) = M(x, y)\mathrm{e}^{\mathrm{i}\varphi(x,y)} \tag{2}$$

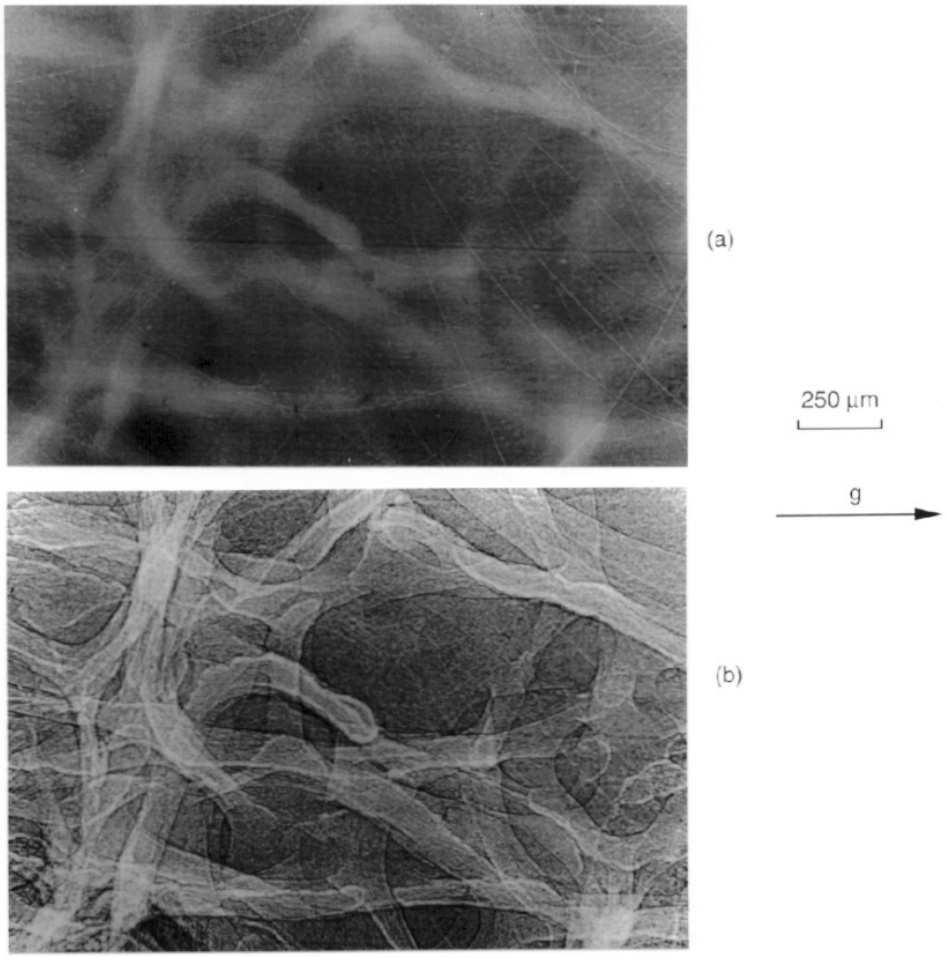

Figure 6. A piece of human vertebra, 7 mm thick, downstream of the monochromator. Image (*b*), based on absorption and phase modulation, reveals new details of the bone structure compared to (*a*), based on absorption: (*a*) $D \approx 0$ cm, (*b*) $D = 100$ cm; symmetric Bragg reflection: 111; $E = 18.8$ keV ($\lambda = 0.66$ Å).

where M describes the absorption and φ the phase modulation, with

$$M(x, y) = \exp\left(-\frac{1}{2}\int \mu(x, y, z)\,\mathrm{d}z\right) \tag{3}$$

$$\varphi(x, y) = \frac{2\pi}{\lambda}\int (n(x, y, z) - 1)\,\mathrm{d}z. \tag{4}$$

μ is the linear absorption coefficient and n the real part of the refractive index. The integrals in (3) and (4) are understood to be along the propagation direction z over the object. This projection of the object in a single plane is justified as long as the propagation in the object is negligible. In expression (4) we suppressed the mean phase modulation in the object because it does not affect the intensity. In the case of x-rays the real part of the refractive index n, for a pure element, depends on the electron density according to [16]

$$n = 1 - (N_0/A)\rho_m r_0(Z + f')\lambda^2 \tag{5}$$

where N_0 is Avogadro's number, A the atomic mass, Z the atomic number, ρ_m the mass per unit volume, $r_0 = 2.8$ fm the classical electron radius, f' the real part of the wavelength-dependent dispersion correction [17] and λ the wavelength. The deviation of this refractive index from unity is very small (less than 10^{-5}). The field in the plane of observation can be calculated in several ways. One possibility is to consider a decomposition into spherical waves of the field after the object, leading to the Fresnel–Kirchhoff diffraction integral and its familiar Fresnel and Fraunhofer approximations. An alternative way is to decompose the field into plane waves and to describe the effect of propagation from sample to film as a linear filter, i.e. to apply Fourier optics.

In general there is no simple relation between the transmission function of the object and the measured intensity $I(x)$ at a point x in the image plane. However for a non-absorbing sample, the Fourier transform of the intensity (see the appendix) can be simply obtained from [18] (limiting ourselves to one dimension for clarity)

$$\tilde{I}(f) = \delta(f) + 2\sin(\pi\lambda D f^2)\tilde{\varphi}(f) \tag{6}$$

if

$$|\varphi(x) - \varphi(x - \lambda D f)| \ll 1 \qquad \forall x. \tag{7}$$

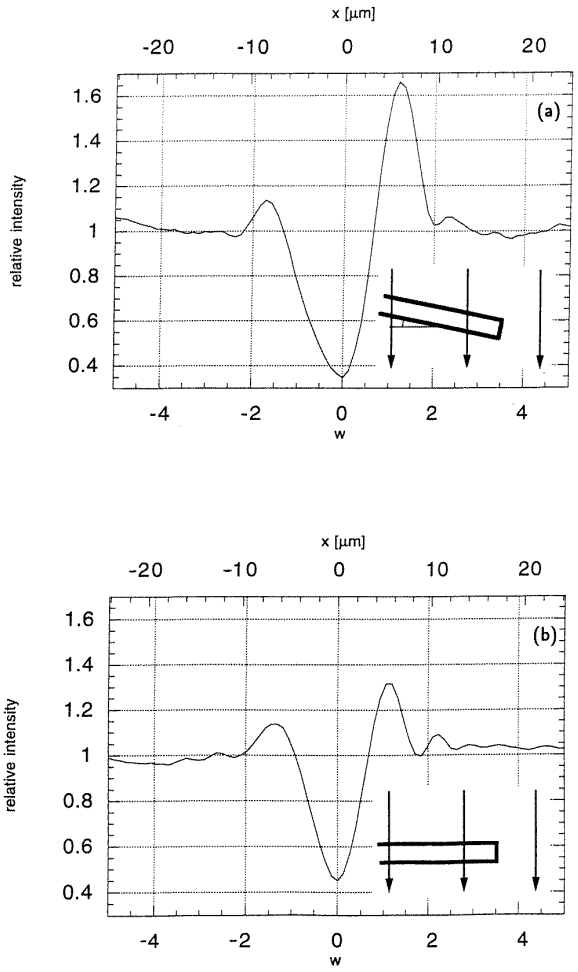

Figure 7. The profile obtained at the edge of a 60 μm thick silicon plate: (*a*) slightly tilted edge (tilt 4.5°) (see inset) and (*b*) perpendicular edge (see inset), corresponding to a phase jump close to $-3\pi/2$. The dimensionless coordinate $w(=\sqrt{2}x/(\lambda D)^{1/2})$ is normally used in Fresnel diffraction phenomena.

Expression (6) is valid for all spatial frequencies f in the case of a weak phase object. $\tilde{I}(f)$ and $\tilde{\varphi}(f)$ denote respectively the Fourier transform of the intensity $I(x)$ and the phase modulation $\varphi(x)$, for the spatial frequency f. $\delta(f)$ is the Dirac distribution and corresponds to a homogeneous background in the image. Expression (6) means that the intensity pattern obtained is selectively sensitive to some spatial frequencies in the phase modulation, according to the value of the factor $2\sin(\pi\lambda D f^2)$ in expression (6). Optimal contrast for the frequency f is obtained when the following condition is met:

$$2\lambda D f^2 \approx 1. \tag{8}$$

A very important parameter turns out to be the radius of the first Fresnel zone, $(\lambda D)^{1/2}$ (in the case in which the source–object distance is much larger than the object–photographic plate distance). The first Fresnel zone around a point of the object gives the part of the object mainly contributing to the intensity in the corresponding point of the image. For the images described above, the size of the first Fresnel zone varies from 0 to typically 8 μm, therefore it is most often smaller than or comparable with the characteristic size of the object. This explains why the image looks more like a direct image of the contours of the object, in which each border is imaged independently, rather than like a hologram, although the experimental set-up is the same as for in-line Gabor holography [19].

2.3. Experimental requirements

For the observation of phase images the incident wave must fulfil monochromaticity and source size conditions, the latter being more severe. An extended source leads to a loss of contrast which can be understood, through a simple geometrical picture, as the convolution of the image for a point source with the projection of the effective source on the film through the sample. The width of this projection is $D\alpha_S$, where the incident divergence α_S equals s/R, with R the distance source object and s the effective size of the source [20]. This implies the following condition for the image corresponding to a spatial frequency f not to be blurred

$$D\alpha_S < 1/f. \tag{9}$$

Eliminating the frequency f by means of expressions (8) and (9), which are respectively the condition to obtain contrast and not to blur it, yields

$$\frac{\lambda}{\alpha_S} > \frac{(\lambda D)^{1/2}}{\sqrt{2}}. \tag{10}$$

Hence, the beam incident on the object must be coherent over the first Fresnel zone and not necessarily over the whole object. This blurring implies that this kind of phase imaging is impossible with classical x-ray sources. At the ESRF, working at a distance of 60 m from the source, the incident divergence α_S is smaller than 5 μrad vertically and 10 μrad horizontally, corresponding to broadenings of 5 and 10 μm at 1 m from the sample. This broadening affects the fine details in the image but does not destroy it completely, as can be seen for the fringes in figures 7(*a*) and (*b*). The better visibility for the horizontal string in figure 3 is related to the smaller vertical source size.

Since the synchrotron radiation beam is initially white, monochromatization must be performed somewhere along the optical system. Setting the object upstream of the monochromating crystal has the practical advantage of providing several images corresponding to different wavelengths in a single exposure. However, the crystal affects the image resolution through the width of the Borrmann fan. For a symmetric Laue reflection this width, projected in the diffracted direction, is $2t\sin\theta_B$, where t is the thickness of the monochromator and θ_B the Bragg angle. When working with a thin crystal and at small θ_B this blurring is often acceptable.

As pointed out by Brauer *et al* [21] the monochromator, even when it is a perfect crystal, can also affect the angular collimation of the beam. Assuming the incident polychromatic beam to be perfectly collimated, the direction of the diffracted beam is slightly wavelength-dependent. The increase in divergence in the plane

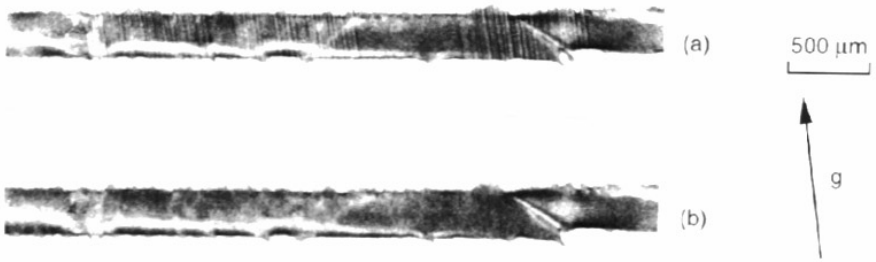

Figure 8. A section topograph of an α-$LiIO_3$ crystal, with an incident beam restricted vertically to about 12 μm by slits. (*a*) A phase object introduced at the slit opening giving rise to streaks parallel to the diffraction vector. (*b*) 'Clean' slits eliminating this contrast. The slit–film distance is 221 cm; white beam section topograph; $8\bar{2}1$ reflection in transmission; E = 30 keV (λ = 0.42 Å).

of diffraction, which can be considered as a chromatic aberration, is given by

$$\alpha_{\Delta\lambda} = \omega_i |1 + b| \tag{11}$$

where ω_i is the width of the intrinsic rocking curve and b is the asymmetry factor defined as $\sin(\delta + \theta_B)/\sin(\delta - \theta_B)$, with δ the angle between the crystal surface and the diffracting lattice planes. This effect vanishes only in symmetric Bragg geometry and was the motivation for our choice of this experimental configuration. For comparison, the divergence introduced by using a symmetric Laue configuration is 18 μrad for a silicon 111 monochromator at 30 keV, hence greater than the divergence α_S of the beam.

Because the mean phase in the object is of no importance, the thickness of the samples that can be investigated is *not* limited to the longitudinal coherence length, which depends on the wavelength spread $\Delta\lambda/\lambda$ through $l_{coh} = \lambda^2/\Delta\lambda$, and is typically only 10 μm at 1 Å for $\Delta\lambda/\lambda = 10^{-5}$. The transmission function F and the phase modulation φ in expression (2) are not affected considerably as long as

$$\Delta t(1 - n)\Delta\lambda/\lambda^2 \ll 1$$

where $\Delta t(1 - n)$ is the maximum fluctuation in optical pathlength in the sample. $(1 - n)$ being very small, the object may be much thicker or the spectral spread larger than in a method directly sensitive to the phase and not to the phase gradients. The Fresnel diffraction effects are not very sensitive to a wavelength variation $\Delta\lambda$ as long as $\Delta\lambda D f^2 \ll 1$, as indicated by expression (6). We conclude that the finite spectral spread $\Delta\lambda/\lambda$ of typically 10^{-5} does not affect the images described above.

3. Topography

3.1. Destroying spurious phase images on x-ray topographs

It is now clear that the visibility of phase objects in the simple set-up used in hard x-ray topographic work at the ESRF is due to the high coherence of the synchrotron radiation beam associated with the low emittance in the machine and the huge source–sample distance.

Spurious phase images disturb not only projection topographs as mentioned in the introduction but also section topographs. Figure 8(*a*) is a section topograph of a 0.4 mm thick α-$LiIO_3$ crystal, obtained at an energy of 30 keV (wavelength 0.42 Å), with the beam restricted to a blade shape by a horizontal slit of vertical height 12 μm. We used the $8\bar{2}1$ reflection and placed the photographic plate and the slits at respectively 21 and -200 cm with respect to the crystal, distances being counted as positive along the beam direction. High-contrast streaks appear when a phase object is introduced at the slit opening. They are parallel to the projection of the diffraction vector, as expected from the broadening of a point on the entrance surface of the crystal to the width of the Borrmann fan at the exit surface. Figure 8(*b*) shows a section topograph of the same crystal, made with clean slits. These stripes on the section topographs appear to be related to dust deposition at the slit edges, probably due to electrostatic effects connected to photoemission.

Phase inhomogeneities such as those due to defects of beryllium windows along the beamline will probably be very difficult to avoid. It is therefore desirable to devise a way of eliminating these images of phase objects. It appears that the possibility that we explored, namely the use of a random phase screen (subsequently referred to as a RPS), also gives the possibility of tailoring the apparent source size, a feature which appears very useful for the future of topography at third-generation synchrotron sources.

Good results were obtained by passing the beam through rotating discs of ash wood a few millimetres thick, cut perpendicularly to the fibre direction and mounted on the shaft of an electric motor. The disc performed several rotations over the exposure time to ensure correct averaging. Figure 9(*a*) shows a transmission (projection) topograph, made at x-ray energy 33.5 keV (wavelength 0.37 Å) in monochromatic mode $(n, -m)$ of a Simox sample without any screen in the beam. For the monochromator and the sample we used respectively a 111 and a 022 reflection. The Simox sample consists of a 540 μm thick silicon substrate with a 0.4 μm thick amorphous SiO_2 layer and a 10 μm thick epitaxic silicon capping layer, obtained through ion implantation and thermal annealing [22]. The images of dislocations, located in the thin silicon layer, appear as dots but, as in figure 1,

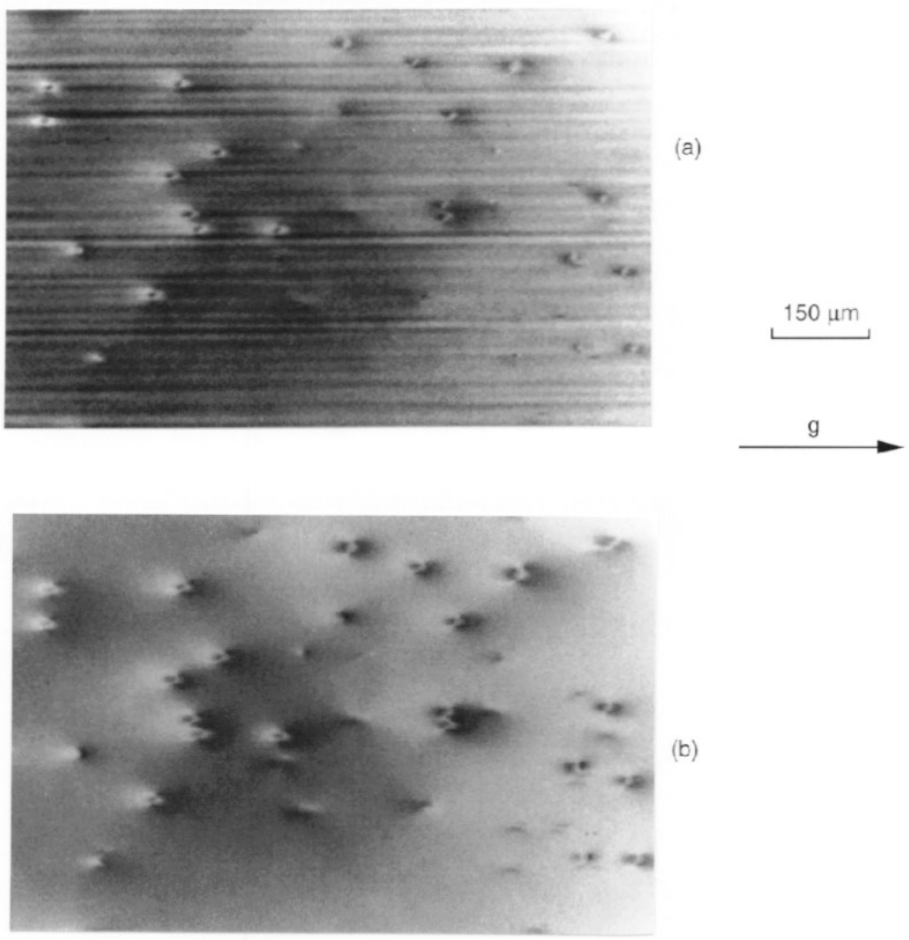

Figure 9. A monochromatic beam topograph of a Simox (see text) sample, 550 μm thick: (*a*) no random phase screen and (*b*) 2 mm thick random phase screen. Dislocations in the top layer are visible in (*a*) as well as corrugations on a beryllium window. The use of the rotating screen in (*b*) blurs completely the phase-image of the beryllium and affects only slightly the image of the dislocations. Some dislocations can only be recognized in (*b*). Distances with respect to the Simox sample: film 17 cm, RPS -220 cm, window -280 cm; reflections in transmission: 111 (monochromator) and 022 (crystal under study); E = 33.5 keV (λ = 0.37 Å).

are perturbed by horizontal lines due to corrugations on the beryllium window. The film, the monochromator and the window were respectively at 17, -125 and -280 cm with respect to the crystal under study. Figure 9(*b*) corresponds to the use of a rotating screen, 2 mm thick, placed -220 cm (upstream) of the crystal. The phase image of the beryllium window is completely smeared out. The dislocation images are only slightly affected, due to the relatively small crystal–film distance of 17 cm.

We tried to verify and to quantify the effect of the thickness of the screen on the coherence properties of the beam. This was achieved by setting two silicon crystals downstream of the screen in (n, n) configuration and by rotating the second one. We worked in transmission geometry with the 111 reflection. Figure 10 shows the rocking curves at x-ray energy 17.7 keV ($\lambda = 0.7$ Å) respectively without any screen, with a 2 mm and a 6.8 mm thick screen. Figure 11 shows the widths of the rocking curves (FWHM) as a function of the screen thickness L for two different energies, 17.7 and 29.5 keV (λ respectively 0.7 and 0.425 Å). Some thicknesses were achieved by assembling two separate screens on a single motor shaft, but no difference was observed compared with the case of a single disc of the same total thickness.

Increasing the incident divergence too much can also deteriorate the topographic image, as shown in figure 12. Figure 12(*a*) corresponds to a 'weak beam' image of a dislocation in a germanium sample obtained at x-ray energy 29 keV with a 111 reflection of a silicon monochromator. The image obtained with a crystal–film distance of 34 cm remains very narrow due to the extremely small apparent source size. Figure 12(*b*) shows the dislocation in the same situation, but with a 4 mm thick screen upstream of the monochromator, leading to an unacceptable broadening of the dislocation image.

This effect can be understood in several closely related ways. Imposing a spatially inhomogeneous time-dependent random phase and averaging the intensity over the exposure time is equivalent to lowering the spatial coherence of the beam, increasing the apparent source size or increasing the incident divergence. For an object downstream of the screen, the screen increases the incident divergence α and

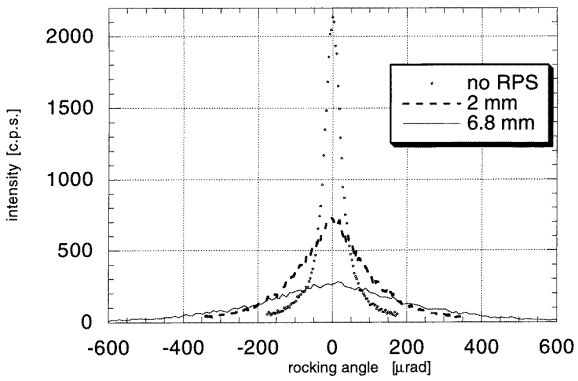

Figure 10. Rocking curves for different thicknesses of the RPS, obtained by setting two silicon crystals in (n, n) configuration downstream with respect to the screen and rocking the second one. 111 reflections in transmission; E = 17.7 keV (λ = 0.7 Å).

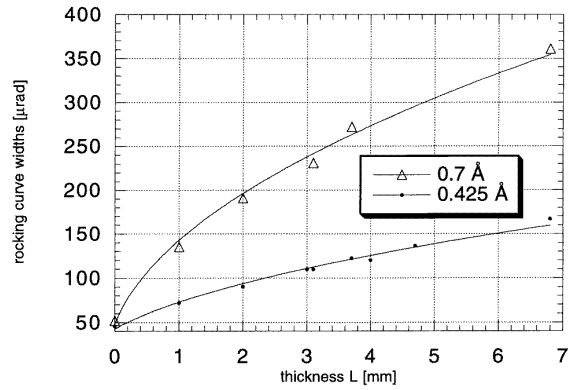

Figure 11. The width of the rocking curves (FWHM) as a function of the thickness of the screen for two energies: E = 17.7 keV (λ = 0.7 Å) and E = 29.5 keV (λ = 0.425 Å).

causes a point blurring of $D\alpha$, where D is the distance between the object and the image plane. If the object is upstream with respect to the RPS (as is the case for the beryllium window discussed previously), theoretical analysis (see the appendix) shows that the principal factor affecting the blurring is the distance between the screen and the image plane. This increase in divergence smears out totally the phase image of the beryllium defects in figure 9(*b*), but affects to a much lesser degree the topographic image of the Simox dislocations because the crystal–film distance is much smaller than the screen–film distance, 17 cm compared with 237 cm.

From figure 11 it is clear that the apparent source size depends in a controllable way on the thickness of the screen, because the refractive index in the screen fluctuates with well-determined statistics. The situation is very similar to that of the propagation of light in a randomly inhomogeneous medium, a problem which has been much investigated in the case of the atmosphere and is discussed in detail in the series by Rytov *et al* [23]. The divergence of the beam passing the screen increases due to statistical refraction and diffraction in the screen. We limit ourselves to the simplifying assumption that only refraction occurs and model the remaining degree of coherence between two points separated by a distance r, denoted by $\gamma_{RPS}(r)$ (see the appendix), of the beam which went through the RPS. The important local characteristic of the medium is the covariance of the refractive index, describing the average way the refractive index fluctuates at two points separated by a lateral distance r, and defined as

$$\psi_n(r) = \langle \delta n(s) \delta n(s+r) \rangle \tag{12}$$

where δn represents the fluctuation from the mean value of the refractive index. This function is expected to decease from its maximum value σ_n^2 (the dispersion of the refractive index) at $r = 0$ to zero at infinite distance, at a rate characterized by the correlation radius l_n. This correlation radius depends only on the geometry of the distribution of inhomogeneities. A fraction p of the beam may remain completely coherent. This fraction (defined as $p = \lim_{r\to\infty} \gamma_{RPS}(r)$) decreases exponentially with the thickness L of the screen.

$$p = \mathrm{e}^{-mL} \tag{13}$$

with

$$m = 8\pi^2 \sigma_n^2 l_n / \lambda^2 \propto \lambda^2 \tag{14}$$

σ_n being proportional to λ^2 because of the wavelength-dependence of the refractive index n as indicated by expression (5).

A common model for the covariance $\psi_n(r)$ is a Gaussian distribution

$$\psi_n(r) = \sigma_n^2 \exp\left(-\frac{r^2}{\pi l_n^2}\right). \tag{15}$$

Under the assumption (15) the degree of coherence takes the form

$$\gamma_{RPS}(r) = \exp\left\{-mL\left[1 - \exp\left(-\frac{r^2}{\pi l_n^2}\right)\right]\right\} \tag{16}$$

which can be written

$$\gamma_{RPS}(r) = \exp\left\{-a\left[1 - \exp\left(-\frac{b}{a} r^2\right)\right]\right\} \tag{17}$$

with two parameters $a = mL$ and $b = mL/(\pi l_n^2)$.

If the coherent fraction tends to zero, namely for a strong random phase screen, the degree of coherence and the angular distribution will also be Gaussian with a transverse coherence length $l_\perp$ of the form [23]

$$l_\perp \propto \frac{\sqrt{l_n}}{\sqrt{L}\sigma_n} \lambda \propto \frac{\sqrt{l_n}}{\lambda\sqrt{L}} \tag{18}$$

and a divergence α_{RPS} of the form

$$\alpha_{RPS} = \frac{2(\ln 2)^{1/2}}{\pi} \lambda \sqrt{b} \propto \sigma_n \left(\frac{L}{l_n}\right)^{1/2} \propto \lambda^2 \left(\frac{L}{l_n}\right)^{1/2}. \tag{19}$$

According to this model, the divergence introduced by the screen increases as the square root of the thickness and it is strongly wavelength-dependent because it increases as the square of the wavelength. This behaviour of the divergence

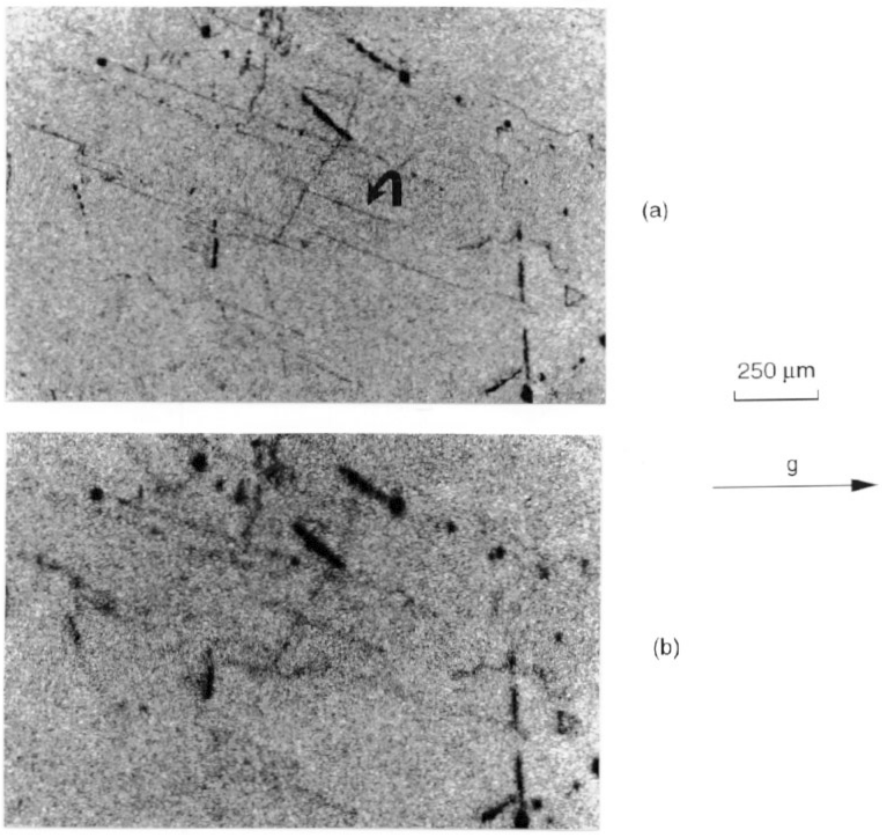

Figure 12. A monochromatic beam topograph of a 325 μm thick germanium sample. Weak beam image of several dislocations (one of which is indicated with an arrow) and some surface defects: (a) no screen and (b) 4 mm thick RPS. The use of a screen which is too strong and a too large crystal–film distance gives strong blurring of the dislocation images. The crystal–film distance is 34 cm; 111 reflections in transmission; E = 29 keV (λ = 0.43 Å).

can also be understood by considering the path of the optical rays in the screen as a Brownian random walk. The number of steps N, namely the number of times that the ray is refracted, is proportional to the thickness of the screen L. The average angle of refraction is zero, but its standard deviation is proportional to σ_n and thus to λ^2. As a result we expect $\alpha_{RPS} \propto \sigma_n\sqrt{N} \propto \lambda^2\sqrt{L}$, as in expression (19).

The intensity as a function of the rocking angle in figure 10 is the convolution of the rocking curve without the screen and the angular distribution introduced by the screen. Using the model above, we deconvolved the rocking curves to obtain separately the contribution of the screen. For each rocking curve, we determined using a least-squares method the two parameters a and b in the general form of the degree of coherence of expression (17); they are defined such that the first characterizes the completely coherent fraction p and the second the divergence of the beam α_{RPS} (FWHM) in the case of a strong screen ($p \approx 0$). Figure 13(a) shows the coherent fraction p as a function of the thickness L of the screen. p decreases as expected but not strictly according to expression (13). Figure 13(b) shows the linear relationship between the divergence α_{RPS} and the square root of the thickness L, as expected from expression (19). The ratio of the slopes at wavelengths respectively 0.7 and 0.425 Å equals 2.75($\pm$0.06), in very good agreement with the value 2.71 expected from the proportionality with the square of the wavelength as indicated by expression (19).

The divergence can also be estimated from the images of the dislocations in the germanium sample in figure 12. Without any screen the width is 5 μm for the dislocation marked with an arrow in figure 12(a), whereas with the screen the width is 20 μm. This leads to an apparent increase in divergence of 60 μrad after deconvolution, which is less than the value of 120 μrad obtained from the rocking curve. However, other dislocations are wider and are hardly visible in figure 12(b). This discrepancy may be related to the focusing–defocusing effect discussed in [24].

3.2. Tailoring beam collimation for topography

The 'diffraction imaging' or 'topography' station of the ESRF, which is under construction, will be located 145 m from a wiggler source. This large distance was chosen in order to have a large enough beam in the vertical direction at the sample position. The beam divergence is expected to be as small as 1.5 μrad and the spectral spread after monochromatization by a perfect single crystal will be smaller than 10^{-5}. This offers many advantages such as easy production of a quasi-plane wave for topography with high angular resolution or the possibility of working with large crystal–film distances (up to 1 m) which

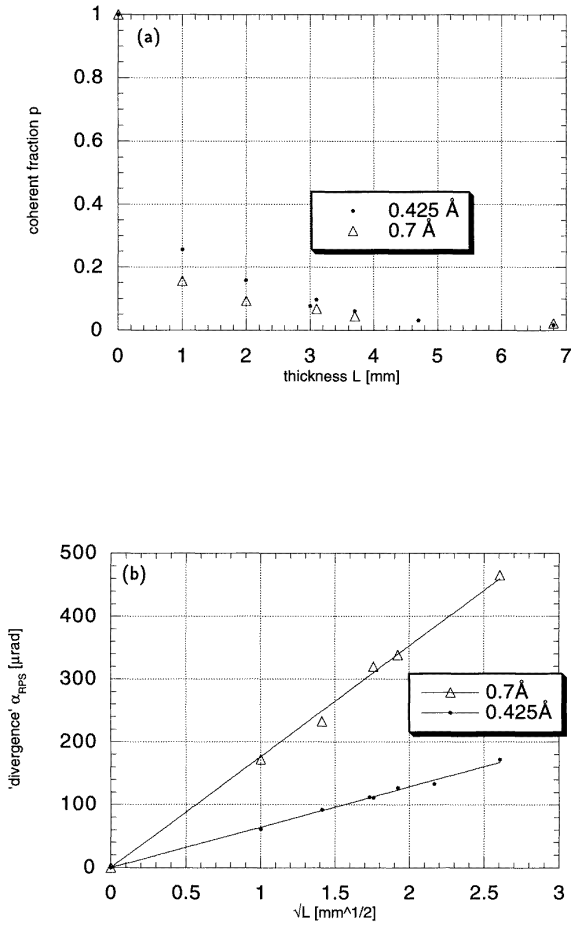

Figure 13. Deconvolution of the rocking curves of figure 10 to obtain the effect of the RPS separately. (*a*) The completely coherent part *p* decreasing with the thickness of the screen *L* and (*b*) 'divergence' (see text) introduced by the screen versus $\sqrt{L}$. The ratio of the slopes of the linear fits is 2.75(±0.06), whereas the ratio of λ^2 is 2.71. E = 17.7 keV (λ = 0.7 Å) and E = 29.5 keV (λ = 0.425 Å).

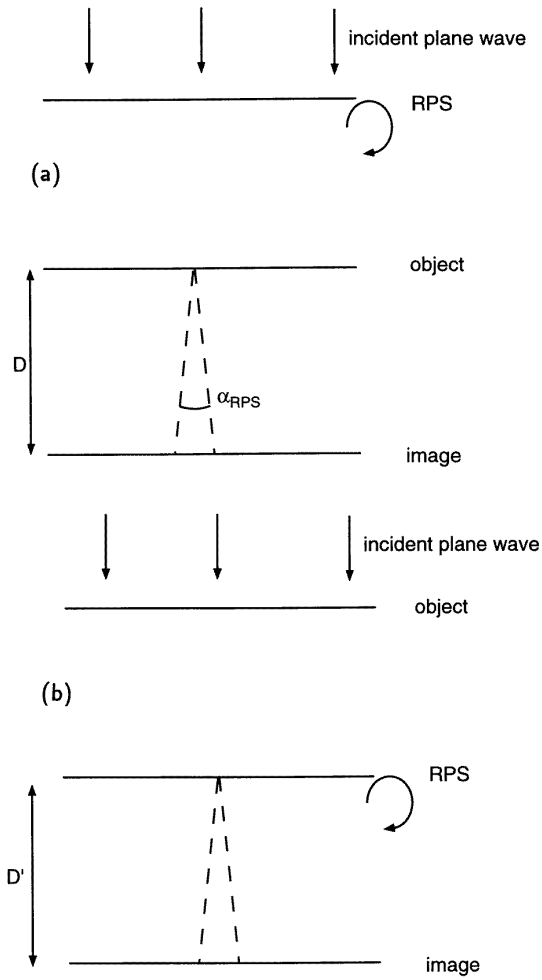

Figure 14. The use of the random phase screen placed upstream (*a*) or downstream (*b*) with respect to the object. The object is characterized by its transmission function $F(x)$; the RPS by the degree of coherence $\gamma_{RPS}(x_1 - x_2)$. D is the object–image plane distance and D' is the screen–image plane distance.

may be required by the sample environment (vacuum or low-temperature devices) without appreciable broadening of the image [25]. On the other hand, these angular and spectral spreads are sometimes too small for the investigation of moderately imperfect crystals, due to the varying Bragg condition in the sample. When working in a monochromatic, dispersive configuration only a small part of the specimen may be imaged because the energy in the monochromatic beam section is position-dependent. The above results show that rotating random phase screens, in addition to eliminating parasitic contrast due to phase objects, can also provide a flexible way of moderately increasing the incident divergence, a feature which can be very useful for some experiments.

4. Conclusions

We have explored some of the features of free-space propagation, or Fresnel diffraction, or defocusing, imaging of phase objects with synchrotron radiation hard x-rays. The small emittance of the ESRF source, resulting in a narrow angular source size and fairly high spatial coherence of the incident beam, is the essential ingredient making observations of this kind possible with extremely simple instrumentation. This method is complementary to other forms of phase imaging that can be performed with hard x-rays, which correspond in the case of light to interferometric contrast [6] and Schlieren imaging [8].

The visibility of fine structure in complex materials is considerably improved in comparison with absorption-based imaging (radiography). Enticing possibilities appear for phase imaging computer-assisted tomography.

Random phase screens have been shown to be an effective way of destroying the phase images when they are artefacts, namely in diffraction imaging (x-ray topography) of defects in single-crystal specimens, through the decrease in coherence, or increase in divergence, of the beam. They should also be useful tools for tailoring the beam in synchrotron radiation topography

Acknowledgments

The authors are happy to thank A Freund and the Optics Group at the ESRF for their cooperation, and A Snigirev for the useful discussions during the early part of this work. We acknowledge the colleagues of the Topography Group for their help, in particular P Rejmánková and E Prieur. We also wish to thank M Pateyron for procuring the vertebra sample and M Ohler for proposing wood as the material for the random phase screen.

Appendix

This theoretical appendix concerns some wave-optical aspects of importance for our study, mainly in the field of Fresnel diffraction of quasi-monochromatic beams with non-ideal spatial coherence properties.

A1. Representing the partial coherence of a quasi-monochromatic beam

A complete description of the beam emitted by a partially coherent source, such as an extended incoherent source, is given by the mutual intensity. The mutual intensity, resulting from incoherent superposition of individual waves of wave-amplitudes $\Psi_z^{(i)}(x)$, where x is the transverse coordinate and z the coordinate along the mean direction of propagation, is defined as

$$J_z(x_1, x_2) = \sum_i \Psi_z^{(i)}(x_1)\Psi_z^{(i)*}(x_2). \tag{A1}$$

For $x_1 = x_2$, we obtain the usual intensity

$$I_z(x) = J_z(x, x). \tag{A2}$$

In the case of an extended incoherent source, the $\Psi_z^{(i)}(x)$ are the wavefunctions of the coherent beams emitted by the different points (i) of the source. Consider, for instance, a source at infinite distance with an angular distribution $S(\beta)$, as seen from the object. The mutual intensity is the same in any observation plane ($z =$ constant), namely

$$J(x_1, x_2) = \int \mathrm{d}\beta S(\beta) \exp\left(\mathrm{i}\frac{2\pi}{\lambda}\beta(x_1 - x_2)\right) = \tilde{S}\left(\frac{x_1 - x_2}{\lambda}\right) \tag{A3}$$

where S and $\tilde{S}$ denote a pair of Fourier transforms.

The degree of coherence γ is the normalized version of $J(x_1, x_2)$

$$\gamma(x_1, x_2) = \frac{J(x_1, x_2)}{[I(x_1)I(x_2)]^{1/2}}. \tag{A4}$$

This degree of coherence determines for example the visibility of the interference fringes formed behind an opaque screen with two identical pinholes.

A2. The Fourier transform $\tilde{I}(f)$ of the intensity distribution $I(x)$ of a Fresnel diffraction image

In terms of mutual intensity the Fresnel transformation is

$$J_D(x_1, x_2) = \frac{1}{\lambda D}\int_{-\infty}^{\infty}\int_{-\infty}^{\infty}\mathrm{d}\eta_1\,\mathrm{d}\eta_2 \times \exp\left(\mathrm{i}\frac{\pi}{\lambda D}[(x_1 - \eta_1)^2 - (x_2 - \eta_2)^2]\right) J_0(\eta_1, \eta_2) \tag{A5}$$

linking the mutual intensity in the $z = D$ plane to the mutual intensity in the $z = 0$ plane. Here we consider the Fourier transform $\tilde{I}(f)$ of the intensity $I(x) = J_D(x, x)$, defined as

$$\tilde{I}(f) = \int_{-\infty}^{\infty}\mathrm{d}x\,\mathrm{e}^{\mathrm{i}2\pi xf} I(x). \tag{A6}$$

Introducing the integral representation of expression (A5) into definition (A6), the triple integral simplifies to a single integral

$$\tilde{I}(f) = \int_{-\infty}^{\infty}\mathrm{d}\eta\, e^{\mathrm{i}2\pi\eta f} J_0\left(\eta + \frac{\lambda Df}{2}, \eta - \frac{\lambda Df}{2}\right). \tag{A7}$$

It is interesting to apply this formula to the case of a phase object with a transmission function $F(\eta) = \mathrm{e}^{\mathrm{i}\varphi(\eta)}$ in the $z = 0$ plane, illuminated by a partially coherent incident beam described by the mutual intensity (A3). We find from (A7)

$$\tilde{I}(f) = \tilde{S}(Df)\int_{-\infty}^{\infty}\mathrm{d}\eta\,\mathrm{e}^{\mathrm{i}2\pi\eta f}\exp\mathrm{i}\left[\varphi\left(\eta + \frac{\lambda Df}{2}\right) - \varphi\left(\eta - \frac{\lambda Df}{2}\right)\right]. \tag{A8}$$

From (A8) we obtain directly the 'weak-phase' approximation

$$\tilde{I}(f) = \tilde{S}(Df)[\delta(f) + 2\sin(\pi\lambda Df^2)\tilde{\varphi}(f)] \tag{A9}$$

with the condition

$$\left|\varphi\left(\eta + \frac{\lambda Df}{2}\right) - \varphi\left(\eta - \frac{\lambda Df}{2}\right)\right| \ll 1 \qquad \forall\eta \tag{A10}$$

which is a less restrictive and more precise condition than the usually stated condition $|\varphi(\eta)| \ll 1$ for any η. The effect of the source is the multiplicative factor $\tilde{S}(Df)$ in expression (A8) and corresponds in direct space to the convolution of the image for coherent illumination with the projection of the angular distribution $S(\beta)$ of the source on the image plane from the object.

A3. The influence of a random phase screen on Fresnel images

A random phase screen is a phase object with a homogeneous random phase $\varphi(x)$ characterized by the correlation function

$$\gamma_{RPS}(x_1 - x_2) = \langle \mathrm{e}^{\mathrm{i}\varphi(x_1)}\mathrm{e}^{-\mathrm{i}\varphi(x_2)}\rangle. \tag{A11}$$

This is the degree of coherence after transmission through the screen of an incident plane wave. The degree of coherence between two points is only dependent upon the distance between the points due to the homogeneity of a

screen in rotation. By means of expression (A3) we can calculate the angular distribution $\tilde{\gamma}_{RPS}(\beta/\lambda)$ of the effective incoherent source resulting from the presence of the RPS. We now consider the effect of the presence of a RPS on the Fresnel diffraction image of an object. Two cases are to be considered.

A3.1. RPS upstream with respect to the object

This situation is schematically represented in figure 14(*a*). The mutual intensity of the beam exiting from the object with a transmission function $F(x)$ is given by

$$J(x_1, x_2) = \gamma_{RPS}(x_1 - x_2)F(x_1)F^*(x_2) \qquad \text{(A12)}$$

where $\gamma_{RPS}(x_1 - x_2)$ does not depend on the RPS–object distance. Using expression (A7) we get the Fourier transform of the intensity on the image plane

$$\tilde{I}(f) = \gamma_{RPS}(\lambda D f)\tilde{I}_{coh}(f) \qquad \text{(A13)}$$

where $\tilde{I}_{coh}(f)$ corresponds to the case without RPS. In direct space, the effect of the RPS is to blur the image by convolution of the 'ideal' image $I_{coh}(x)$ with the projection of the angular distribution $\tilde{\gamma}_{RPS}(\beta/\lambda)$ on the image plane from the object. The width of the projection is $D\alpha_{RPS}$, where α_{RPS} is the width of the angular distribution and D is the object–image plane distance.

A3.2. RPS downstream with respect to the object

This situation is schematically represented in figure 14(*b*). Now we have to apply first a Fresnel transformation of $F(x)$ from the object to the screen, giving the amplitude distribution $\Psi(x)$ just before the screen. The mutual intensity just after the RPS is

$$J(x_1, x_2) = \gamma_{RPS}(x_1 - x_2)\Psi(x_1)\Psi^*(x_2) \qquad \text{(A14)}$$

We apply a second Fresnel transformation over the RPS–image plane distance D'. Applying expression (A7), the contribution of the RPS can be factored out to give

$$\tilde{I}(f) = \gamma_{RPS}(\lambda D' f)\tilde{I}_{coh}(f). \qquad \text{(A15)}$$

The effect of the RPS is entirely in the first term. $\tilde{I}_{coh}(f)$ corresponds again to the case without RPS because two successive Fresnel transformations, from object to screen and from screen to image, are equivalent to a single Fresnel transformation over the object–image plane distance D. The important difference with respect to the first case is that now the blurring effect due to the RPS is related to the projection of the angular distribution from the screen to the image plane over the distance D'.

References

[1] Sayre D and Chapman H N 1995 *Acta Crystallogr.* A **51** 237–52

[2] Schmahl G, Rudolph D, Guttmann P, Schneider G, Thieme J and Niemann B 1995 *Rev. Sci. Instrum.* **66** 1282–6

[3] Lang A R 1978 *Diffraction and Imaging Techniques in Material Science* 2nd edn, ed S Amelinckx *et al* (Amsterdam: North-Holland) p 623

[4] 1987 *Proc. Second World Conf. on Neutron Radiography, Paris* (Dordrecht: Reidel)

[5] Baruchel J 1993 *Neutron and Synchrotron Radiation for Condensed Matter Studies* vol I, ed J Baruchel *et al* (Berlin: Springer) p 399

[6] Ando M and Hosoya S 1972 *Proc. 6th Int. Conf. on X-ray Optics and Microanalysis* ed G Shinoda *et al* (Tokyo: University of Tokyo Press) p 63

[7] Schlenker M, Bauspiess W, Graeff W, Bonse U and Rauch H 1980 *J. Magn. Magn. Mater.* **15–18** 1507–9

[8] Förster E, Goetz K and Zaumseil P 1980 *Kristall Technik* **15** 937–45

[9] Davis T J, Gao D, Gureyev T E, Stevenson A W and Wilkins W 1995 *Nature* **373** 595–8; 1995 *Phys. Rev. Lett.* **74** 3173–6

[10] Podurets K M, Somenkov V A, Chistyakov R R and Shilushtein S Sh 1989 *Physica* B **156–157** 694–7

[11] Snigirev A, Snigireva I, Suvorov A, Kocsis M and Kohn V 1995 *ESRF Newsletter* no 24 June 23–5
Snigirev A, Snigireva I, Kohn V G and Kuznetsov S M 1995 *Nucl. Instrum. Methods* at press; 1995 *Rev. Sci. Instrum.* at press

[12] Cowley J M 1975 *Diffraction Physics* 2nd edn (Amsterdam: North-Holland) p 59

[13] Goetz K and Zaumseil P 1979 *Habilitationsschrift* and *PhD Thesis* Jena

[14] Lenz F 1961 *Z. Phys.* **164** 425–7

[15] Born M and Wolf E 1980 *Principles of Optics* 6th edn (Oxford: Pergamon)

[16] Parrat L G 1954 *Phys. Rev.* **95** 359

[17] 1992 *International Tables for Crystallography* vol C (Dordrecht: published for the International Union of Crystallography by Kluwer Academic Publishers) p 206

[18] Guigay J P 1977 *Optik* **49** 121–5

[19] Jacobsen C, Kirz J, Howells M, McQuaid K, Rothman S, Feder R and Sayre D 1988 *X-ray Microscopy II* ed D Sayre *et al* (Berlin: Springer) p 253
Joyeux D, Lowenthal S, Polack F and Bernstein A 1988 *X-ray Microscopy II* ed D Sayre *et al* (Berlin: Springer) p 246

[20] Coïsson R 1995 *Appl. Opt.* **34** 904–8

[21] Brauer S, Stephenson G B, Sutton M, Mochrie S G J, Dierker S B, Fleming R M, Pindak R, Robinson I K, Grübel G, Als-Nielsen J and Abernathy D L 1995 *Rev. Sci. Instrum.* **66** 1506–9

[22] Prieur E, Härtwig J, Garcia A, Ohler M, Baruchel J, Aspar B and Rolland G 1995 *J. Cryst. Growth* at press

[23] Rytov S M, Kravtsov Yu A and Tatarskii V I 1989 *Principles of Statistical Radiophysics* vol 3 and 4 (Berlin: Springer)

[24] Zontone F, Mancini L, Barrett R, Baruchel J, Härtwig J and Epelboin Y 1995 *J. Synchrotron Radiat.* submitted

[25] Barrett R, Baruchel J, Härtwig J and Zontone F 1995 *J. Phys. D: Appl. Phys.* **28** A250–5